Skillful Wintertime North American Temperature Forecasts out to 4 Weeks Based on the State of ENSO and the MJO*

NATHANIEL C. JOHNSON

International Pacific Research Center, School of Ocean and Earth Science and Technology, University of Hawai'i at Mānoa, Honolulu, Hawaii, and Scripps Institution of Oceanography, University of California, San Diego, La Jolla, California

DAN C. COLLINS

NOAA/NCEP/Climate Prediction Center, College Park, Maryland

STEVEN B. FELDSTEIN

Department of Meteorology, College of Earth and Mineral Sciences, The Pennsylvania State University, University Park, Pennsylvania

MICHELLE L. L'HEUREUX

NOAA/NCEP/Climate Prediction Center, College Park, Maryland

EMILY E. RIDDLE

NOAA/NCEP/Climate Prediction Center, College Park, Maryland, and Wyle Information Systems, McLean, Virginia

(Manuscript received 29 August 2013, in final form 25 October 2013)

ABSTRACT

Previous work has shown that the combined influence of El Niño–Southern Oscillation (ENSO) and the Madden–Julian oscillation (MJO) significantly impacts the wintertime circulation over North America for lead times up to at least 4 weeks. These findings suggest that both the MJO and ENSO may prove beneficial for generating a seamless prediction link between short-range deterministic forecasts and longer-range seasonal forecasts. To test the feasibility of this link, wintertime (December–March) probabilistic 2-m temperature (T2m) forecasts over North America are generated solely on the basis of the linear trend and statistical relationships with the initial state of the MJO and ENSO. Overall, such forecasts exhibit substantial skill for some regions and some initial states of the MJO and ENSO out to a lead time of approximately 4 weeks. In addition, the primary ENSO T2m regions of influence are nearly orthogonal to those of the MJO, which suggests that the MJO and ENSO generally excite different patterns within the continuum of large-scale atmospheric teleconnections. The strong forecast skill scores for some regions and initial states confirm the promise that information from the MJO and ENSO may offer forecasts of opportunity in weeks 3 and 4, which extend beyond the current 2-week extended-range outlooks of the National Oceanic and Atmospheric Administration's (NOAA) Climate Prediction Center (CPC), and an intraseasonal link to longer-range probabilistic forecasts.

1. Introduction

Operational weather forecasters face the ongoing challenge of bridging the "predictability gap" between short-range deterministic weather forecasts and longer-range probabilistic monthly and seasonal climate forecasts. For lead times of approximately 10 days or less, forecasts are based on the initial atmospheric conditions

* International Pacific Research Center Publication Number 1023 and School of Ocean and Earth Science and Technology Contribution Number 9029.

Corresponding author address: Nathaniel Johnson, IPRC, University of Hawai'i at Mānoa, 401 POST Bldg., 1680 East–West Rd., Honolulu, HI 96822.
E-mail: natj@hawaii.edu

DOI: 10.1175/WAF-D-13-00102.1

and are determined through integrations of numerical weather prediction (NWP) models. For lead times of approximately 1 month or more, forecasts, in contrast, are based on slowly varying boundary conditions (e.g., sea surface temperature and soil moisture anomalies) and are often determined through a blend of numerical model integrations and statistical models. For intermediate lead times of approximately 10–30 days, however, the large growth of initial errors and the insufficient time for boundary conditions to take effect present significant difficulties in generating a seamless prediction framework that links the short-range daily weather forecasts with monthly and seasonal climate forecasts.

A source of hope, however, has been the numerous recent studies that detail the significant influence of the Madden–Julian oscillation (MJO) on the extratropical circulation, particularly during winter, in this 1–4-week time frame. The MJO, which is the dominant form of tropical variability on intraseasonal time scales, is characterized by large-scale convection anomalies that circumnavigate the tropical belt in approximately 30–70 days (Madden and Julian 1971, 1972; Zhang 2005). The MJO tropical convection anomalies excite large-scale teleconnection patterns, including the two dominant Northern Hemisphere patterns: the Pacific–North American (PNA) pattern (Knutson and Weickmann 1987; Ferranti et al. 1990; Higgins and Mo 1997; Mori and Watanabe 2008; Johnson and Feldstein 2010; Riddle et al. 2013) and the North Atlantic Oscillation (NAO)/Arctic Oscillation (AO) (Cassou 2008; L'Heureux and Higgins 2008; Lin et al. 2009; Roundy et al. 2010; Riddle et al. 2013). These large-scale teleconnections, which are identified in the sea level pressure and geopotential height fields, modify temperature and precipitation patterns over North America (Vecchi and Bond 2004; Lin and Brunet 2009; Lin et al. 2010; Zhou et al. 2012; Yoo et al. 2012; Rodney et al. 2013; Schreck et al. 2013). The MJO-related composite temperature and precipitation patterns over the United States can be viewed at the National Oceanic and Atmospheric Administration's (NOAA) Climate Prediction Center (CPC) website (http://www.cpc.ncep.noaa.gov/, under the MJO section).

One of the fundamental underlying mechanisms by which tropical convection, such as that associated with the MJO, excites PNA-like teleconnection patterns is through the linear dispersion of a Rossby wave triggered by the tropical heating (Hoskins and Karoly 1981; Sardeshmukh and Hoskins 1988; Jin and Hoskins 1995). In addition, barotropic amplification near jet-exit regions (Simmons et al. 1983; Branstator 1985; Hsu 1996; Feldstein 2002) and driving by synoptic eddies (Moore et al. 2010; Franzke et al. 2011) contribute to the observed amplitude and preferred geographic location of the PNA over the North Pacific and North America. The mechanisms by which the MJO excites the NAO/AO over the North Atlantic basin are more uncertain, but such mechanisms likely involve modification of the upstream storm track and background flow by the MJO, which impacts the Rossby wave breaking that gives rise to the NAO/AO (Benedict et al. 2004; Cassou 2008). Because the extratropical response takes approximately 1–2 weeks to become established (Jin and Hoskins 1995; Matthews et al. 2004), and because MJO convection exhibits consistent eastward propagation on weekly time scales, the MJO provides the potential to aid extended-range forecasts for lead times of approximately 1–4 weeks (Ferranti et al. 1990; Newman and Sardeshmukh 2008; Brunet et al. 2010; Gottschalck et al. 2010; Johnson and Feldstein 2010; Vitart and Molteni 2010; Jones et al. 2011; Riddle et al. 2013; Hoskins 2013; Zhang 2013).

In addition to the MJO-related anomalies, tropical convection anomalies associated with El Niño–Southern Oscillation (ENSO), which is the dominant mode of tropical atmosphere–ocean interaction on interannual time scales, also excite large-scale teleconnection patterns with significant weather impacts over North America (Ropelewski and Halpert 1987; Halpert and Ropelewski 1992; Trenberth and Caron 2000). Several studies find that ENSO may modulate the extratropical response to the MJO (Schrage et al. 1999; Tam and Lau 2005; Roundy et al. 2010; Moon et al. 2011; Riddle et al. 2013), which suggests that the state of both ENSO and the MJO should be considered to maximize the potential of skillful forecasts in this 1–4-week window. A few of these studies (Schrage et al. 1999; Roundy et al. 2010; Moon et al. 2011) indicate that the combined MJO and ENSO influence is not a simple linear combination of the separate responses, although Riddle et al. (2013) finds linearity to be a reasonable approximation for the combined effect of the MJO and ENSO on the frequency of PNA-like geopotential height cluster patterns. Both ENSO and the MJO excite PNA-like patterns, although with some differences in their spatial structure, which suggests that the MJO and ENSO excite different members of the PNA continuum (Johnson and Feldstein 2010). Whereas the MJO has a significant impact on the NAO/AO, a similar link has not been observed between ENSO and the AO (L'Heureux and Thompson 2006).

Although the aforementioned studies suggest the potential for the MJO to contribute to skillful extended-range forecasts over North America, little work has been done to assess the practical usefulness of MJO information as guidance for operational, probabilistic forecasts. Yao et al. (2011) and Rodney et al. (2013) find that surface air temperature forecasts based on statistical relationships with two of the eight Wheeler and Hendon (2004, hereafter WH04) MJO phases in particular (phases 3 and 7) provide modest skill over southern Canada and the northern United States at a lead time of 10–20 days. Both MJO phases are characterized by an east–west dipole of tropical convection, where phase 3 (phase 7) features enhanced (suppressed) convection over the tropical Indian Ocean and suppressed (enhanced) convection over the central equatorial Pacific Ocean. Despite the evidence of skill, Yao et al. (2011) doubt that such a statistical model could be of practical use in operational forecasting because the resulting correlations with surface air temperature were modest. Rodney et al. (2013), in contrast, suggest that potentially useful forecasts for days 6–15 are possible during MJO phases 3, 4, 7, and 8, but only during strong MJO episodes. Neither study, however, considered the possible combined influence of the MJO with ENSO. In addition, the strong long-term linear trend of wintertime surface air temperature over regions of North America (e.g., Lee et al. 2011) provides another possible source of skill. Therefore, the combined influence of the MJO, ENSO, and linear trend may enable ''forecasts of opportunity,'' which are periods characterized by higher than usual forecast skill that may be of practical benefit to some regions beyond a 10-day lead time. The purpose of this study is to evaluate the potential usefulness of a statistical, probabilistic forecast model of North American, wintertime surface air temperatures based on the initial state of the MJO and ENSO and on the linear trend in the 1–4-week time frame. We generate probabilistic temperature forecasts for weekly periods, with lead times out to 6 weeks for the December–March winter season between 1980 and 2010. Overall, we find that statistical relationships between North American temperature and the MJO and ENSO may be used to generate forecasts with skill that exceed the typical skill of NWP models for some locations and for some phases of the MJO at lead times of 2–4 weeks, which extend beyond the current NOAA CPC operational forecast products. As discussed below, these forecasts of opportunity exist for approximately three to four active MJO phases, depending on the lead time and the state of ENSO, which corresponds with approximately 25%–30% of all winter days.

The remainder of the article is organized as follows. Section 2 presents the data and methods for generating and evaluating the forecasts. Section 3 presents example temperature forecasts and the forecast evaluation results. Section 4 follows with discussion and conclusions.

2. Data and methodology

In this section we present all data sources and the methodology for generating and then evaluating wintertime temperature forecasts over North America.

a. Data sources

To generate temperature forecasts, we use December–March daily 2-m temperature (T2m) data derived from the Interim European Centre for Medium-Range Weather Forecasts (ECMWF) Re-Analysis (ERA-Interim; Dee et al. 2011) for the period from 1980 through 2010. We focus on land grid points in the domain from 10° to 77.5°N and from 180° to 50°W, which includes all of North America. We interpolate the ERA-Interim 1.5° latitude–longitude grid onto a coarser 2.5° latitude–longitude grid, which does not affect the large-scale features that are the focus of this study. We also examine lagged composites of ERA-Interim 500-hPa geopotential height anomalies on the original 1.5° latitude–longitude grid over the Pacific–North American region from 20° to 90°N and from 160°E to the Greenwich meridian. We calculate daily T2m and 500-hPa geopotential height anomalies by subtracting the seasonal cycle, which is defined as the first four harmonics of the calendar day means for 1981–2010, and then calculate 7-day running mean anomalies.

We assess the initial state of the MJO at the time of issuing forecasts with the WH04 MJO index, as provided by the Australian Bureau of Meteorology (http://cawcr.gov.au/staff/mwheeler/maproom/RMM/). This index is defined by the two leading principal components (PCs) from an empirical orthogonal function analysis of the combined tropical outgoing longwave radiation, 850-hPa equatorial zonal wind, and 200-hPa equatorial zonal wind fields. These two PCs, designated as the real-time multivariate MJO index (RMM) 1 and RMM2, define eight MJO phases and an MJO amplitude, which together describe the eastward propagation of the enhanced MJO convection from the African continent (phase 1) to the central equatorial Pacific Ocean (phases 7 and 8). The OLR and zonal wind composites associated with each phase of the WH04 index can be found in a number of previously published papers (e.g., WH04; Cassou 2008; Johnson and Feldstein 2010) and are also available on the NOAA/CPC website (http://www.cpc.ncep.noaa.gov/, within the MJO section).

We also partition the initial state into three canonical ENSO categories: La Niña, neutral ENSO, and El Niño conditions. We define each category following the conventions of NOAA/CPC. First, we obtain the 3-month running mean values of the Niño-3.4 sea surface temperature (SST) index from the CPC for the period of 1980–2010. This index is defined by the SST anomaly averaged over the region extending from 5°S to 5°N and from 120° to 170°W. Then, we classify an El Niño (La Niña) episode when the 3-month running mean Niño-3.4 SST anomaly is greater than 0.5°C (less than −0.5°C) for at least five consecutive overlapping, 3-month seasons. All other periods are classified as neutral ENSO.

Although we focus on forecasts generated with historical MJO, ENSO, and linear trend information, we also calculate T2m skill scores for a set of 45-day retrospective forecast simulations (hindcasts) from version 2 of the National Centers for Environmental Prediction's (NCEP's) Climate Forecast System model (CFSv2) to establish a skill benchmark from a state-of-the-art NWP model. The CFSv2 model (Saha et al. 2014) consists of the NCEP Global Forecast System (GFS) atmospheric model run at T126 (~0.937°) horizontal resolution and is fully coupled with ocean (Geophysical Fluid Dynamics Laboratory Modular Ocean Model, version 4.0), land surface (Noah land surface model), and sea ice models. The retrospective forecasts are initialized at 6-h intervals from 1999 through 2009 and run out for 45 days. Ensemble means are calculated from the four runs initialized during each 24-h period. Anomalies are calculated by subtracting the ERA-Interim T2m seasonal cycle, as described above, but with the additional step of subtracting the model climatology bias (i.e., the difference between the lead-dependent model climatology and the ERA-Interim climatology for the same period). Also as above, we focus on 7-day running mean anomalies over the North America domain for all forecasts that verify between December and March.

b. Generation of probabilistic temperature forecasts over North America

We generate weekly probabilistic T2m forecasts with verification centered on all days in December–March from 1980 to 2010 for six different weekly lead times, days 4–10, and weeks 2–6. The first lead time is chosen to correspond with the NOAA/CPC 6–10-day outlook, but expanded to a 7-day window, and the second lead time corresponds exactly with the CPC's 8–14-day outlook. We follow the standard CPC format of forecasting the probability of above and below average temperatures, where above (below) average temperatures are defined by the top (bottom) terciles of the climatological (1981–2010) temperature distribution for the particular 7-day calendar period. For the generation of the forecasts, the T2m anomaly tercile boundaries at each grid point are determined by pooling all December–March T2m anomalies in the training data, described below, and then calculating the 33.33rd and 66.67th percentiles of the T2m anomaly data. For the forecast evaluation described in section 2c, however, the verified forecast category is based on the distribution of the 30 T2m anomalies from 1981 to 2010 for the specific 7-day calendar period, as in the NOAA/CPC's 8–14-day outlooks.

The forecasts at each 2.5° grid cell are generated based on historical temperature distributions, conditional on the initial state of ENSO and the MJO. To calculate conditional distributions, we partition the initial state on each day by the phase of the MJO and ENSO. We define the initial state of the MJO by the WH04 MJO phase under the condition that the RMM amplitude exceeds 1.0, designated as MJO episodes (65% of all December–March days meet this criterion); all days below this amplitude threshold are used to create a "weak MJO" forecast category. The mean skill scores show little change if this amplitude threshold is increased to 1.25 or 1.5, and so we keep the lower, more inclusive threshold. We recognize that such a simple definition will designate some periods as active that are not "pure" MJO episodes (i.e., with the characteristic eastward progression), but we choose this simple criterion for two main reasons. First, for real-time forecasts, the forecaster does not have the luxury of determining whether a given MJO episode candidate will propagate as a pure MJO episode after the time of issuing the forecast. Second, even if the episode is not a pure MJO episode, the associated convection may generate a similar extratropical response (e.g., Roundy and Gribble-Verhagen 2010). We also partition by the three phases of ENSO discussed above.

For the combination of the MJO and ENSO influence, we considered two possibilities. First, if the modulation of the MJO impacts by ENSO is substantially nonlinear (Roundy et al. 2010; Moon et al. 2011), then we should consider partitioning the initial state into separate joint MJO–ENSO categories. However, with nine different MJO states (eight MJO phases and weak MJO) and three different ENSO states, the consideration of 27 different joint MJO–ENSO categories would result in fairly small sample sizes with which to calculate each conditional temperature distribution. Alternatively, if the nonlinearity is sufficiently weak, then we may obtain a more robust forecast using larger sample sizes by assuming independent impacts and linearly superimposing the expected ENSO and MJO effects. We tried both strategies and found that forecasts with the assumption of linearity outperformed the forecasts based on partitioning into separate MJO/ENSO categories. Even after trying several modifications to increase sample sizes, such as joining multiple MJO phases into a single category, we found the assumption of linear superposition to result in forecasts with higher skill scores. These results do not mean that the relationship between ENSO and the MJO is purely linear, but rather they suggest that any nonlinearity evident in the Northern Hemisphere temperature composites is not strong enough to overcome the additional sampling uncertainty that results from smaller sample sizes. Therefore, we assume a linear superposition of the MJO and ENSO influence for our final forecasts.

To generate the forecasts, we use a leave-one-year-out cross-validation approach; that is, the forecasts in year y are based on the statistics from data in all years excluding year y, denoted as the training data. We make the following calculations at each grid point, g, for each of the six lead times, t, included in this study (t = 7, 11, 18, 25, 32, and 39 days for the 4–10-day and week-2 through week-6 forecasts, respectively). First, we use the training data to calculate conditional means and variances of detrended T2m anomalies associated with each of the nine initial MJO states, i (eight "active" MJO phases, and one "weak" MJO state), and three initial ENSO states, j. We denote these as μ_{tig} and σ^2_{tig}, for the mean and variance conditional on the MJO, and μ_{tjg} and σ^2_{tjg}, for the mean and variance conditional on ENSO. Note that these means and variances are independent of the calendar day, and that the mean seasonal cycle has been removed previously when calculating T2m anomalies. Next, we assume that the ENSO and MJO impacts are independent, as discussed above, and add the two means and variances: $\mu_{tg} = \mu_{tig} + \mu_{tjg}$ and $\sigma^2_{tg} = \sigma^2_{tig} + \sigma^2_{tjg}$. To account for the long-term trend, we then add back in the linear trend to μ_{tg}; the linear trend for the December–March 1980–2010 period is shown in Fig. 1. The ERA-Interim T2m trends compare favorably with other observations-based datasets (not shown). Differences from other published studies (e.g., Bukovsky [2012]) are mainly due to differences in the precise months and years analyzed. With the assumption that the T2m anomalies follow a Gaussian distribution with mean μ_{tg} and variance σ^2_{tg}, we calculate the probability that T2m will fall in the top (bottom) tercile to produce the forecast for above (below) average T2m at grid point g and lead time t. A schematic of the forecast calculation is shown in Fig. 2. We make this calculation for all available years, lead times, and grid points.

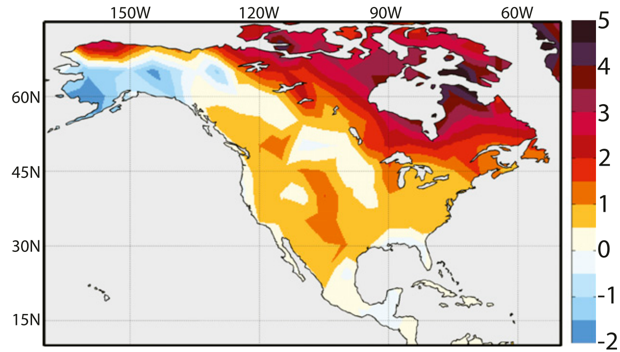

FIG. 1. Linear trend [°C (30 yr)$^{-1}$] of December–March T2m for the period of 1980–2010.

The assumption of a Gaussian T2m distribution is an obvious simplification that does not hold at all times and locations. This assumption is likely least appropriate over northwestern North America, where the T2m distributions are negatively skewed owing to the

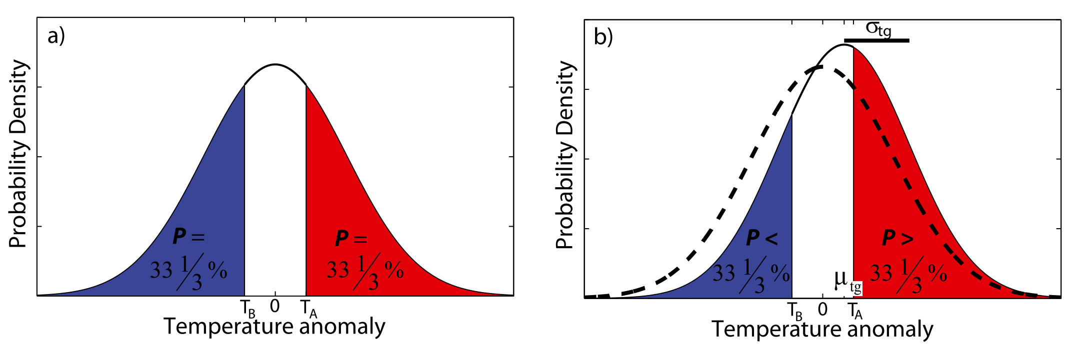

FIG. 2. Schematic of the T2m forecast calculation for grid point g and lead time t. (a) Climatological December–March T2m anomaly distribution from the training data, with tercile boundaries, T_B and T_A. The area shaded in blue (red) represents the probability of below (above) average T2m, which is 33 ⅓% in climatology by definition. Note that this schematic assumes a Gaussian climatological distribution, but the actual calculation of tercile boundaries does not assume any parametric parent distribution. (b) Forecast T2m anomaly distribution with mean μ_{tg} and standard deviation σ_{tg} (solid curve), assumed Gaussian and conditioned on the initial state of the MJO and ENSO (see text for details). The climatological T2m anomaly distribution is dashed. The forecast probability of above (below) average T2m is represented by the area shaded above T_A in red (below T_B in blue), which indicates an enhanced (suppressed) probability of above (below) average T2m relative to climatology.

modifying influence of the Pacific Ocean (not shown). However, we find that skill scores are relatively high over this region (section 3), and test forecasts based on the training data frequency of occurrence rather than on an assumed Gaussian distribution do not show notable differences in mean skill scores. Therefore, the Gaussian assumption does not appear to hurt skill scores appreciably.

We also calculate lagged composites of 7-day-mean 500-hPa geopotential height anomalies for select initial MJO and ENSO phases in order to examine the connection between the T2m forecasts and the large-scale midtropospheric circulation. To determine statistically significant geopotential height anomalies, we use a Monte Carlo resampling procedure, whereby we repeat the composite calculations 10 000 times but with random draws from the entire pool of geopotential height data. These draws are determined by randomly reassigning the year and calendar day of each field in the original composite. The calendar day reassignment is performed through a single random and circular shift in the calendar day between −60 and +60 days for all identified events of a given year. Then, we identify the actual composite anomalies that fall outside the 95% confidence interval from the resampled composites to define statistically significant anomalies. We choose this approach to generate a random distribution of composites that retains the sample sizes and autocorrelation of the geopotential height anomaly data associated with individual MJO episodes that span several consecutive days within a given year.

c. *Forecast evaluation*

We evaluate all forecasts with the Heidke skill score (HSS), a common performance metric used by the CPC to evaluate extended-range probabilistic forecasts (e.g., Wilks 2011). The HSS assesses the proportion of categories forecast correctly. For the forecasts generated with historical MJO, ENSO, and trend information, each probabilistic forecast is assigned to one of the three forecast categories (top, middle, or bottom tercile) based on the highest of the three forecast probabilities. For the CFSv2 forecasts, the assigned category is based on the deterministic four-member ensemble mean forecast. The number of categories forecast correctly is designated as H. The expected number of categories forecast correctly just by chance, E, is one-third of the total number of forecasts, T, for this three-category case. The HSS then can be expressed as

$$\mathrm{HSS} = \frac{(H - E)}{(T - E)} \times 100. \qquad (1)$$

The HSS ranges in value from −50 (completely wrong set of forecasts) to 100 (perfect set of forecasts), with zero as the expected HSS for a randomly generated forecast. A value of zero also can be considered the expected HSS of a climatological forecast if we define a climatological forecast as a random draw from three equiprobable forecast categories. Therefore, HSS values above zero indicate that the forecasts have at least some skill.

We assess the statistical significance of the HSS for the forecasts generated with historical MJO, ENSO, and trend information through a Monte Carlo resampling test similar to that of the 500-hPa geopotential height anomaly composites. In this case, we perform the same HSS calculations 500 times but with randomly resampled forecasts and verification fields chosen in the same way as in the geopotential height significance test described above. Observed HSS values that are greater than the 95th percentile of the resampled HSS values are deemed statistically significant at the 5% level. Therefore, we perform a two-tailed test for the geopotential height composites, where we test whether the composite anomalies are different from zero, but we perform a one-tailed test for the HSS, where we test if the skill scores are greater than zero. We also evaluate the reliability of the probabilistic forecasts by calculating calibration functions (e.g., Wilks 2011) for each forecast lead time. We make these calculations by binning the forecast probabilities over all days and grid points for a particular lead time and then calculating the frequency of occurrence of the verified category within each forecast probability bin. In contrast with standard reliability diagrams, which contain separate plots of the calibration function and relative frequency of each forecast probability bin, we incorporate forecast bin frequency directly into the calibration function by specifying that each forecast bin represents 10% of all forecasts. This modification allows us to evaluate the sharpness of the forecasts, or the degree to which forecasts deviate from climatological predictions (i.e., how often and to what degree the forecast probabilities differ from the climatological tercile probabilities of 33.3%), directly within the calibration function plot.

3. Results

The forecasts generated by the method described above have three potential sources of skill: the MJO influence, the ENSO influence, and the long-term trend. To illustrate how each of these three sources contributes to the mean skill averaged over North America, we show in Fig. 3a the mean HSS for all winter days between 1980 and 2010 from forecasts generated in four different

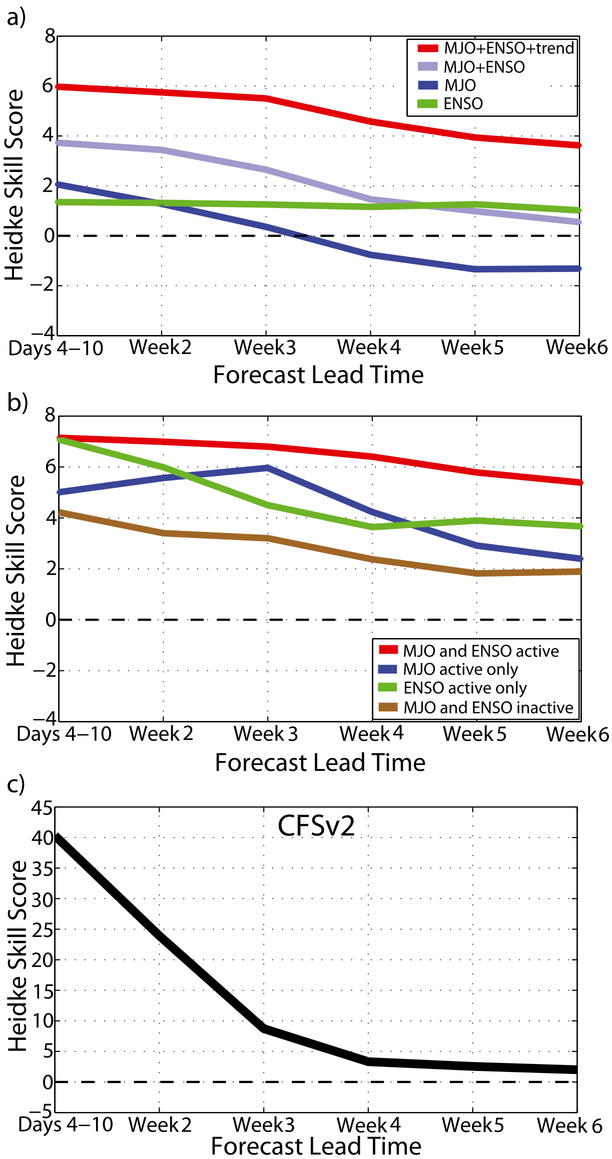

FIG. 3. (a) Mean T2m HSSs averaged over North America and over all winter days as a function of lead time for forecasts based on the initial state of ENSO only (green), the initial phase of the MJO only (dark blue), the combined initial state of the MJO and ENSO (light blue), and the combined initial state of the MJO and ENSO and the linear trend (red). (b) Mean HSSs for forecasts based on the combined initial state of the MJO and ENSO and the linear trend but when ENSO alone is active (green), the MJO alone is active (blue), both the MJO and ENSO are active (red), and both the MJO and ENSO are inactive (brown). The mean numbers of forecasts for each of the four categories are 696, 1064, 1324, and 668, respectively. (c) As in (a) and (b), but for all CFSv2 retrospective forecasts between 1999 and 2009. Note that the scale of the *y* axis in (c) differs from those in (a) and (b).

ways. First, the dark blue curve shows the mean HSS for forecasts generated in the same general way described in section 2 but with only the MJO influence included in the forecasts. We see positive though modest skill scores gradually decreasing from days 4–10 through week 3 and then falling below zero by week 4, indicating that week 4 forecasts based solely on MJO information are worse than random forecasts. These results suggest that the MJO contributes to skillful forecasts until about week 4, when the MJO signal likely is weaker than the noise associated with sampling uncertainty. Forecasts generated with ENSO information only, shown in green, provide nearly constant, weakly positive skill scores from weeks 1 through 6, which is consistent with the longer time scale of ENSO relative to the MJO. The HSS for forecasts that consider both MJO and ENSO information, shown in light blue, approximately equals the linear combination of the MJO-only and ENSO-only HSSs. Therefore, not only do the forecasts assume a linear superposition of the MJO and ENSO influence, but the skill scores also are approximately linear. This light blue curve suggests that the MJO provides additional useful T2m forecast information until week 4, when the ENSO and MJO+ENSO HSS curves become indistinguishable. The addition of the linear trend, shown in red, adds skill at all lead times. The linear trend term adds the greatest skill over the Arctic regions of northeast Canada, where the 31-yr linear trend is strongest (Fig. 1).

It bears mention that the HSSs in Fig. 3a are modest, particularly at shorter lead times, relative to the typical HSSs from NWP models. The CFSv2 mean HSS in Fig. 3c diminishes from ~40 in days 4–10 to about 10 by week 3, before leveling off at an HSS of around 2 or 3 in weeks 4–6. We note, however, that the calculations for Fig. 3a incorporate all winter days, including initial times when the MJO and ENSO are inactive, and all North American locations, including those that are not strongly impacted by either the MJO or ENSO. As discussed below, the mean HSSs from the forecasts presented here exceed the typical HSSs of NWP models for some regions and for some MJO and ENSO initial states for lead times between weeks 2 and 6. Figure 3b presents the mean HSSs from the forecasts that include the MJO and ENSO initial states and the linear trend but only for initial times when ENSO alone is active (green), the MJO alone is active (blue), both the MJO and ENSO are active (red), and both the MJO and ENSO are inactive (brown). As expected, the skill scores are higher when the MJO and ENSO are active. When the MJO alone is active, the skill scores peak in week 3 and decline quickly thereafter. When ENSO alone is active, we surprisingly see the highest skill scores during days 4–10, with a decline and leveling off thereafter; however, the sample size for this category is relatively low (680–731 total forecasts, depending on lead time, versus 1028–1337 total forecasts for the active categories), and so we

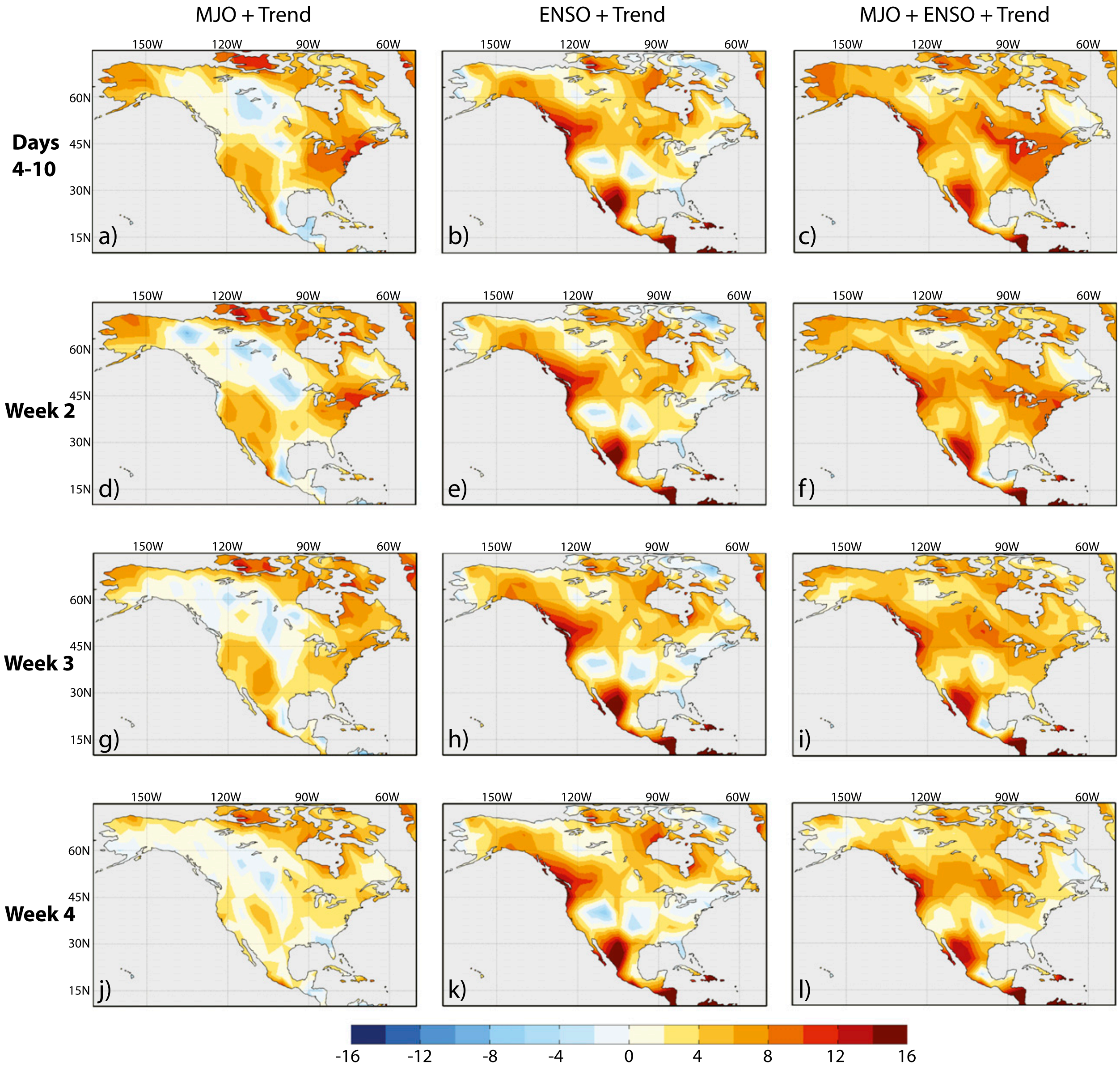

FIG. 4. Gridded mean T2m HSSs for all winter days from forecasts based on (a),(d),(g),(j) the initial state of the MJO and linear trend, (b),(e),(h),(k) the initial state of ENSO and the linear trend, and (c),(f),(i),(l) the initial state of the MJO and ENSO and the linear trend. The corresponding lead times are (a)–(c) days 4–10, (d)–(f) week 2, (g)–(i) week 3, and (j)–(l) week 4.

suspect that a deviation from a flat curve simply may be the result of sampling variability. The width of the 90% confidence interval for the active ENSO mean HSS from the Monte Carlo resampling tests is about 7 at all lead times, which demonstrates the large sampling variability of the HSS in this category. Another possible contributor, however, is that ENSO episodes sometimes decay in late winter, bringing the onset of neutral ENSO conditions by February or March, and our long-lead-time forecasts do not capture this transition. When both the MJO and ENSO are active, the mean HSSs are highest and show only a gradual decline from days 4–10 to week 6, and the HSSs are statistically significant at all lead times.

The MJO and ENSO influence on North American temperatures also exhibits pronounced regional variations. Figure 4 presents the gridded mean HSS for forecasts based on the initial state of the MJO and linear trend (left column), the initial state of ENSO and the linear trend (middle column), and initial state of both the MJO and ENSO and the linear trend (right column). Interestingly, even though both the MJO and ENSO influence North American temperatures through teleconnection patterns excited by tropical Pacific convection anomalies, the MJO and ENSO primarily impact different regions of North America. The left column in Fig. 4 suggests that the MJO most strongly influences temperatures in the northeastern United States and southeastern Canada, southwestern North America, and northern Alaska. A large region of weak skill scores extends across all of western and central Canada. In contrast, the influence of ENSO (Fig. 4, middle column) is strong over western Canada, but weak over the intermountain west and northeast regions of the United States, where the MJO influence is strongest. The primary region of overlapping influence is the southwestern United States and northern Mexico. This contrast in influence is consistent with the idea that both the MJO and ENSO excite PNA-like patterns, but the MJO and ENSO excite different parts of the PNA continuum (Johnson and Feldstein 2010), particularly during El Niño episodes (Riddle et al. 2013). In particular, Johnson and Feldstein (2010) find that El Niño (La Niña) episodes tend to excite easterly (southerly) displaced positive (negative) PNA-like patterns, but the MJO tends to excite canonical PNA-like and western Pacific–like teleconnection patterns. The contrast over eastern North America is likely the result of the significant relationship between the MJO and the NAO/AO that is absent between ENSO and the NAO/AO, as discussed in the introduction, because the NAO/AO has a significant relationship with eastern North America temperatures (Hurrell et al. 2003; L'Heureux and Higgins 2008).

Consistent with Fig. 3, the pattern of mean HSS from the MJO and linear-trend-based T2m forecasts is strongest in days 4–10 and week 2, and then declines in strength in week 3 (Fig. 4g) and especially in week 4 (Fig. 4j). As expected, the mean HSSs from the ENSO and linear-trend-based T2m forecasts show a nearly constant pattern between weeks 1 and 4 (middle column in Fig. 4). The mean HSSs from the forecasts that combine the MJO and ENSO influence with the linear trend (right column in Fig. 4) show more widespread coverage of positive skill scores that combine the MJO and ENSO influence regions. Therefore, Fig. 4 confirms that the state of both the MJO and ENSO are of similar importance for wintertime, intraseasonal T2m forecasts over North America.

Figures 3 and 4 consider all phases of the MJO, but the strength of the relationship between the MJO and North American temperatures varies by the phase of the MJO. Several recent studies (Lin and Brunet 2009; Lin et al. 2010; Yao et al. 2011; Rodney et al. 2013) suggest that the strongest North American MJO impacts occur when there is a pronounced east–west dipole of tropical convective heating anomalies, as occurs during MJO phases 3 and 7. In particular, Lin et al. (2010) use a primitive equation model to show that oppositely signed tropical convective heating anomalies near 80° and 160°E each produce an extratropical response over the North Pacific and downstream North America that reinforces each other, which supports earlier work indicating a change in sign of the Northern Hemisphere response when tropical heating crosses a nodal point near 120°E (Simmons et al. 1983; Ting and Sardeshmukh 1993). Consistent with these results, Schreck et al. (2013) show that the strongest North American temperature anomalies at a lag of 6–10 days occur after MJO phases 3 and 8. In broad support of this perspective, Fig. 5a, which presents the mean HSSs averaged over North America in a Hovmöller-like form for all MJO episodes, indicates that the highest skill scores generally occur in close relation with MJO phases 3 and 7, with suppressed skill scores between these two phases. For example, the enhanced skill scores about 10 days after the occurrence of MJO phase 3 agree with the findings of Yao et al. (2011). However, in contrast with Yao et al. (2011) and Rodney et al. (2013), who only emphasize the potential MJO-related predictability out to 15–20 days, Fig. 5a suggests that the enhanced skill scores extend to much longer lead times of about 4 weeks. One possible contributor to this difference is that Yao et al. (2011) and Rodney et al. (2013) only focus on MJO phases 3, 4, 7, and 8, which primarily project onto one MJO EOF pattern, but some of the enhanced skill scores at longer lead times occur at other MJO phases that project onto both MJO EOFs that define the WH04 phases.

The corresponding week 2 mean T2m forecast after MJO phase 3, presented in the standard format of NOAA/CPC extended-range outlooks (Fig. 6a), and the associated midtropospheric circulation (Fig. 6c) also agree well with recent studies (Lin and Brunet 2009; Yao et al. 2011). Figure 6a is constructed by taking the mean of all week 2 forecasts when the initial state of the MJO is in phase 3, and so the ENSO and linear trend forecast influence should average to near zero; however, the mean HSS (Fig. 6b) contributed by ENSO and the trend should not average out because the skill scores in the regions of strong ENSO influence and linear trend are generally positive in both ENSO phases and over the entire 31-yr period. The forecast map features enhanced probabilities of above average T2m over southeast Canada and the northeast United States, consistent with the pattern reported in Lin and Brunet (2009) and Yao et al. (2011), and enhanced probabilities of below average T2m over western North America, particularly over Alaska. The large-scale circulation associated with

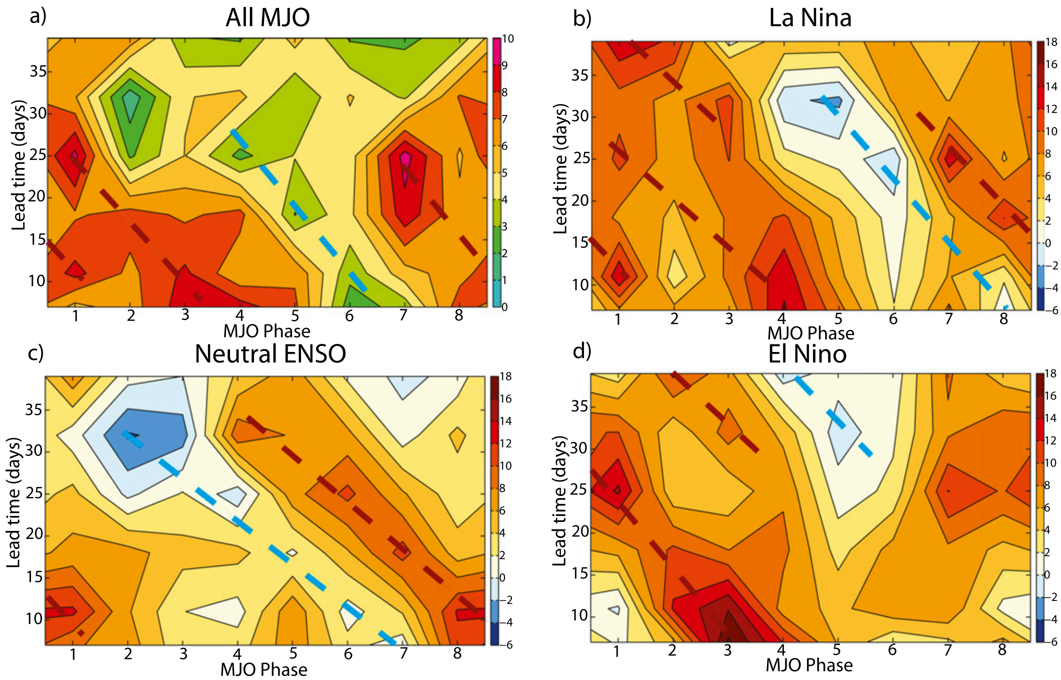

FIG. 5. North America mean T2m HSSs as a function of lead time (y axis) and MJO phase (x axis) for (a) all MJO episodes, (b) MJO episodes during La Niña events, (c) MJO episodes during neutral ENSO conditions, and (d) MJO episodes during El Niño events. The dashed dark red (blue) lines indicate axes of enhanced (suppressed) skill with phase progression that are consistent with the eastward progression of the MJO, as determined by visual inspection of the plots. The assigned day on the y axis corresponds with the central day of the weekly forecast; i.e., y = 7, 11, 18, 25, 32, and 39 days corresponds with the 4–10-day and week-2 through week-6 forecasts, respectively.

this T2m forecast pattern appears to project weakly onto the negative phase of the PNA and more strongly onto the positive phase of the western Pacific patterns, with a low-over-high geopotential height dipole over the North Pacific region (Fig. 6c), consistent with a sea level pressure (Johnson and Feldstein 2010) and geopotential height (Riddle et al. 2013) cluster pattern that is shown to occur more frequently after MJO phase 3. A similar dipole that projects onto the positive phase of the NAO/AO is evident over the North Atlantic, with a pronounced ridge over northeast North America, where the highest probabilities of above average T2m exist. The enhanced probability of occurrence of the positive phase of the NAO/AO 8–14 days after MJO phase 3 is consistent with several recent studies (Cassou 2008; Lin et al. 2009; Roundy et al. 2010). The peak HSSs over northeast North America range from about 15 to 30 (Fig. 6b), which are at least comparable to the mean HSSs from state-of-the-art NWP models at this lead time (e.g., Fig. 3c).

The maximum skill scores associated with MJO phase 7 evident in Fig. 5a actually occur at longer lead times than those of MJO phase 3, as they are found at lead times of 3 and 4 weeks. Figures 6d–f show the mean T2m forecast, HSS, and 500-hPa geopotential height anomaly patterns for week 4 forecasts corresponding with an MJO phase 7 initial state. The forecast pattern (Fig. 6d) features a broad swath of enhanced probabilities of below average T2m extending from Alaska and northwest Canada to the eastern United States. The associated 500-hPa geopotential height anomalies describe high-over-low dipole patterns over the North Pacific and North Atlantic basins, the latter projecting onto the negative phase of the NAO/AO. The negative NAO-like pattern is consistent with the enhanced probability of occurrence of a negative NAO/AO-like cluster pattern approximately 5–25 days after the occurrence of MJO phase 7 (Riddle et al. 2013). The highest skill scores generally occur over the eastern United States (Fig. 6e), coincident with statistically significant negative geopotential height anomalies (Fig. 6f), but statistically significant skill scores extend across a broad region of North America. We note that the precise values of the peak HSS, which range from about 15 to 25, likely overestimate the true skill somewhat due to sampling variability, even in cross-validated forecasts (Kumar 2009). Even with this consideration, these peak skill

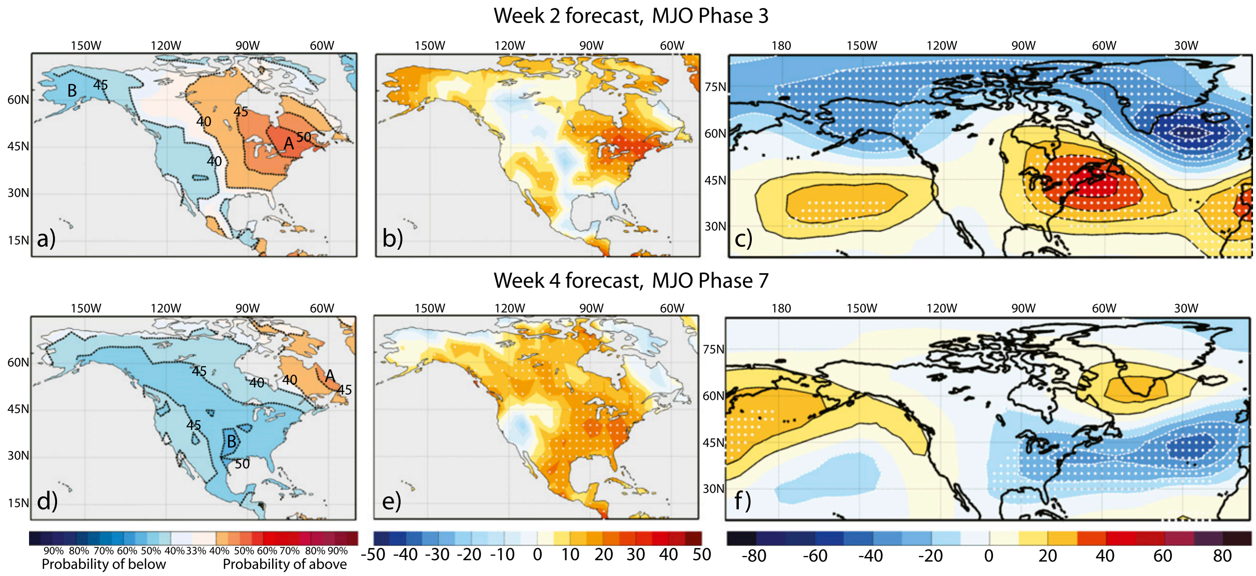

FIG. 6. (a),(d) Mean probabilistic T2m forecast, (b),(e) mean HSSs, and (c),(f) lagged composite 500-hPa geopotential height anomalies (m) for (a)–(c) week 2 forecasts when the initial state of the MJO is phase 3 and for (d)–(f) week 4 forecasts when the initial state of the MJO is phase 7. In (a) and (d) warm (cold) colors correspond with the probability of T2m in the top (bottom) tercile, and probabilities equal to or greater than 40% are contoured in intervals of 5%. In (c) and (f) geopotential height anomalies are contoured at intervals of 10 m, with the zero contour omitted. Stippling in (b),(c),(e), and (f) indicates anomalies that are statistically significant at the 5% level on the basis of a Monte Carlo resampling test described in the text.

scores clearly far exceed the typical week 4 HSSs from NWP models (e.g., Fig. 3c).

Figure 5a also shows enhanced week 4 skill scores after the occurrence of MJO phase 1. The corresponding forecast and circulation anomalies (not shown) are quite similar to the MJO phase 3 patterns depicted in Figs. 6a and 6c. This similarity suggests that the enhanced skill scores in weeks 3 and 4 after MJO phase 1, which extend beyond the 2-week time scale for the extratropics to respond to MJO-related tropical heating (Jin and Hoskins 1995; Matthews et al. 2004), are associated with the same MJO phase 3 episodes that give rise to the circulation anomalies evident in Fig. 6c. Therefore, the unusually high skill scores after week 2, based on expectations from tropical–extratropical interaction theory, likely relate to the consistent propagation of MJO-related tropical convection, as supported by the well-defined axes of enhanced and suppressed HSSs in Fig. 5. Another possible contributor to the enhanced skill scores after week 2 is the recently documented influence of the MJO on the stratospheric polar vortex, with downward-propagating circulation anomalies that eventually project onto the tropospheric NAO/AO over the course of several weeks (Garfinkel et al. 2012). An examination of this possibility is reserved for a future study.

When we also partition the HSS by La Niña (Fig. 5b), neutral ENSO (Fig. 5c), and El Niño (Fig. 5d) episodes, we generally see similar patterns of enhanced and suppressed skill scores, as in the all-MJO episode calculations (Fig. 5a), although the axes of these high and low skill scores tend to be somewhat shifted in phase compared with Fig. 5a. Figure 7 presents three additional mean forecast examples arbitrarily selected from the more deeply shaded orange axes of higher skill in Figs. 5b–d: the week 3 forecast when the initial state is MJO phase 8 and La Niña (Fig. 7a), the week 3 forecast when the initial state is MJO phase 2 and El Niño (Fig. 7d), and the week 4 forecast when the initial state is MJO phase 6 and neutral ENSO conditions (Fig. 7g). Overall, we find strong similarity among the initial MJO phase 2 and 3 (Figs. 6a and 7d) and MJO phase 6–8 (Figs. 6d, 7a, and 7g) forecast groups. The main influence of ENSO on the forecast is to increase the forecast probabilities over western North America, consistent with the ENSO influence regions indicated in Fig. 4. For example, when comparing Fig. 7d with Fig. 6a, we see that El Niño increases the probability of above average (below average) T2m over western Canada and southern Central America (southwestern North America), in agreement with the canonical influence of El Niño on North American surface temperatures (e.g., Halpert and Ropelewski 1992). A similar but oppositely signed influence of La Niña can be discerned by comparing Fig. 7a with Fig. 6d. In the 500-hPa geopotential height field, ENSO exerts a strong influence on the North Pacific anomalies, with El Niño (La Niña) contributing to an

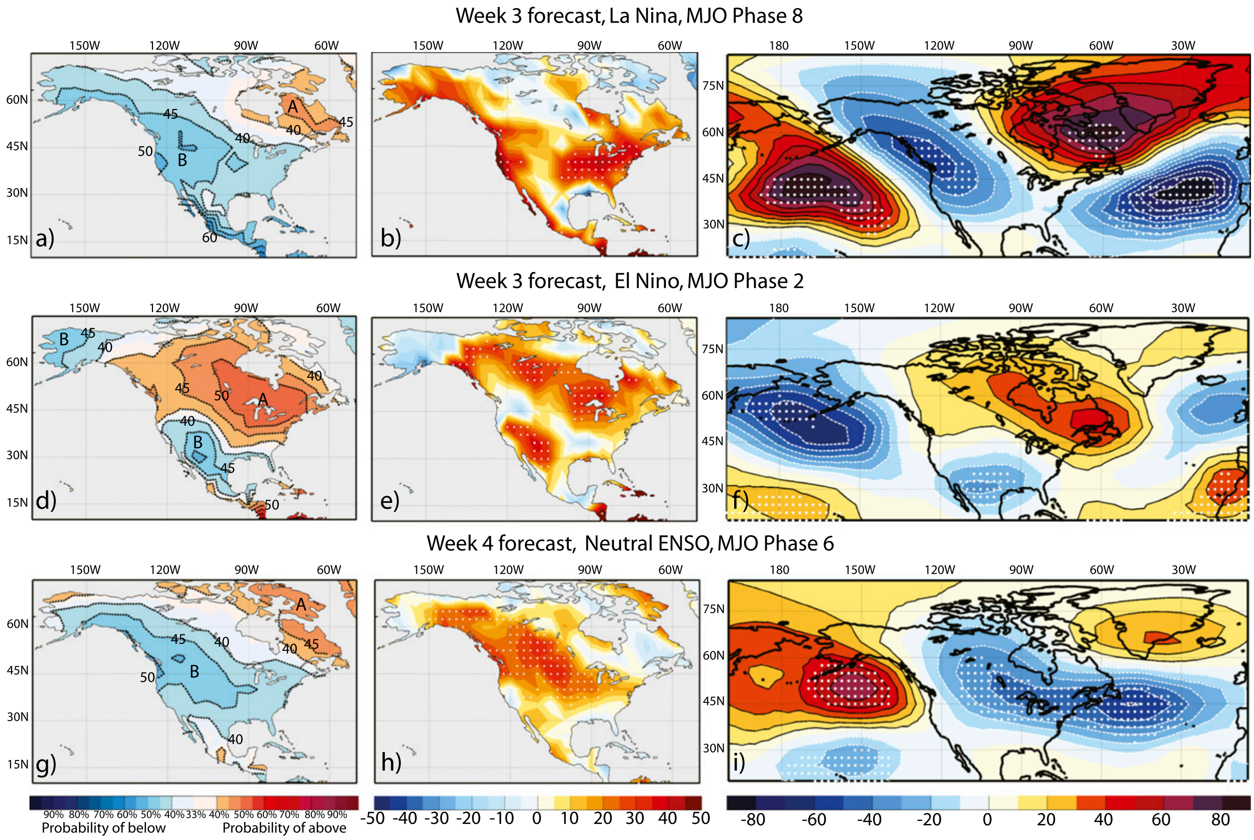

FIG. 7. As in Fig. 6, but for forecasts and lagged composites also conditioned on the initial state of ENSO: (a)–(c) week 3 forecasts when the initial state is La Niña and MJO phase 8, (d)–(f) week 3 forecasts when the initial state is El Niño and MJO phase 2, and (g)–(i) week 4 forecasts when the initial state is neutral ENSO and MJO phase 6.

anomalously strong (weak) Aleutian low, as evidenced in Fig. 7f (Fig. 7c). These patterns are consistent with the known tendency of El Niño (La Niña) to excite the positive (negative) phase of the PNA (e.g., Trenberth et al. 1998). Some differences are also evident in the North Atlantic circulation as well. For example, in the third week after La Niña and MJO phase 8, the westward-displaced negative NAO-like pattern (Fig. 7c) is much stronger than the negative NAO-like pattern in the third week after all MJO phase 8 episodes (not shown), which agrees with the strengthened relationship between the MJO and the NAO during La Niña episodes reported in Roundy et al. (2010). Given that ENSO has only a weak influence over the North Atlantic circulation, this observation suggests a possible nonlinear relationship between the MJO and ENSO in the excitation of North Atlantic teleconnection patterns, but more in-depth analysis is beyond the scope of the present study and reserved for future work.

The regions of highest skill scores in Fig. 7, which generally occur in the regions with the strongest temperature signal, feature HSSs between approximately 20 and 40, with a few locally higher peaks. These week 3 and week 4 skill scores are more typical of the 1–2-week lead time skill scores from dynamical forecast models like the CFSv2 (Fig. 3c). Given that such skill scores are consistent with those of current operational extended-range outlooks out to 2 weeks, the analysis presented here suggests that there are forecasts of opportunity at least to a lead time of 4 weeks when the MJO and ENSO influences on North American temperatures are strong enough to be of practical benefit to operational forecasters. The results of Fig. 5 suggest that these forecasts of opportunity may exist for approximately three or four of the eight WH04 MJO phases, with the number and particular phases depending on the lead time and state of ENSO.

Finally, we briefly comment on the reliability of the forecasts presented here. The calibration functions look quite similar for each lead time, and so we illustrate the week 3 forecast calibration functions in Fig. 8 as a representative example. Overall, the forecasts generally are somewhat overconfident, as exemplified by the slope of the calibration functions in Figs. 8a and 8b, which is less

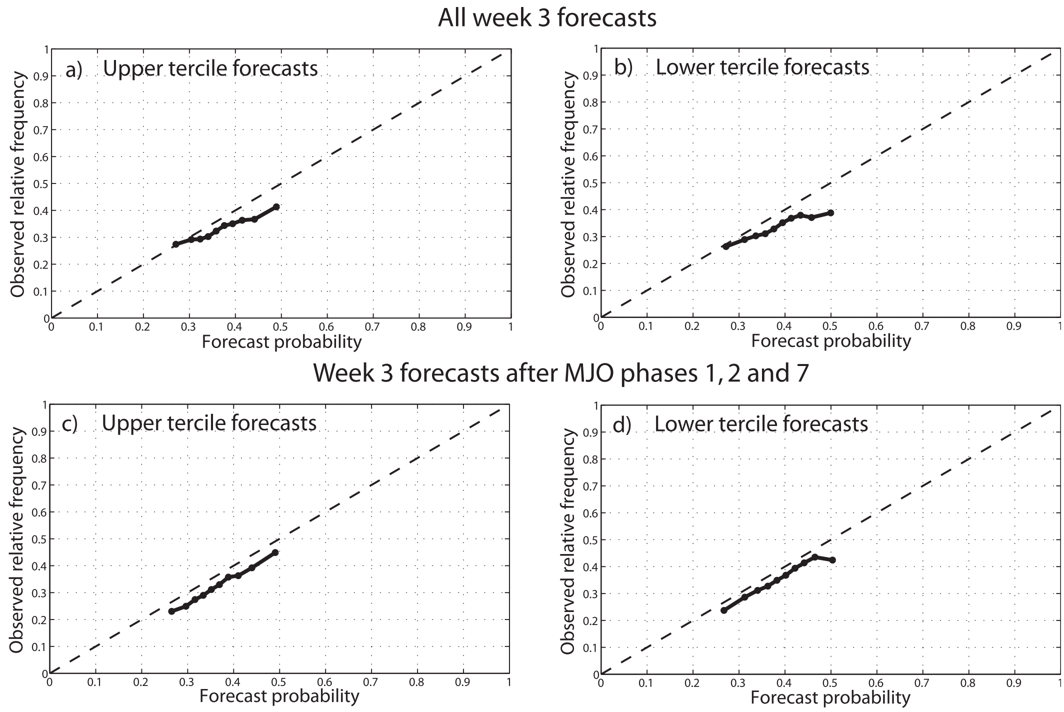

FIG. 8. Calibration functions for (a),(c) top and (b),(d) bottom tercile T2m forecasts corresponding with (a),(b) all week 3 forecasts and (c),(d) week 3 forecasts after the initial state of the MJO is phase 1, 2, or 7. Each point along the line segment within the diagram represents a forecast probability bin center for a bin that contains 10% of the forecasts for the corresponding category.

than one. We suspect that the large number of forecast parameters, given the relatively short data record, and possibly nonstationary MJO–ENSO relationships contribute to this overconfidence. However, we find that if we isolate the initial states that provide the strongest relationship with North American temperatures, the reliability improves substantially. For example, Figs. 8c and 8d show considerably improved week 3 calibration functions, indicating close correspondence between category forecast probability and category frequency of occurrence, after isolation of MJO phases 1, 2, and 7, which are located along the axes of higher skill scores in Fig. 5a. Therefore, we believe that the forecasts generated in the manner described in section 2 are reasonably well calibrated, as long as we restrict our focus to the MJO phases with the strongest relationship to North American temperatures.

4. Discussion and conclusions

In this study we use a simple forecasting approach based on statistical relationships between North American temperatures and both the MJO and ENSO to demonstrate the potential of skillful wintertime temperature forecasts for lead times between 1 and 6 weeks. For some regions and initial MJO phases, the forecast skill scores in weeks 3 and 4 are higher than the typical NWP skill scores in weeks 1 and 2, which indicates that the MJO, when combined with ENSO and the long-term trend, may provide an intraseasonal link to bridge short-range forecasts with monthly and seasonal probabilistic forecasts.

Both the MJO and ENSO have a significant influence on North American temperatures, but the primary MJO and ENSO regions of influence are generally distinct, indicating unique teleconnection patterns excited by the MJO and ENSO. In this study we assume that the MJO and ENSO influence is independent because forecasts that assume linear superposition of T2m impacts have higher skill scores than forecasts that partition the initial state into separate joint MJO–ENSO categories. Although the general relationship between MJO phase and skill score does not depend strongly on the initial state of ENSO (Fig. 5), which supports the linearity assumption, our analysis provides some evidence that the interaction between the MJO and ENSO is not purely linear. The 500-hPa geopotential height composites (Figs. 6 and 7) hint that any nonlinearity may be most pronounced with the North Atlantic teleconnection patterns, as supported by Roundy et al. (2010)

and Riddle et al. (2013). However, the limited data record, which is constrained by the availability of satellite data since only the late 1970s, makes it challenging to account for any nonlinearity without overfitting the forecast model and harming the temperature predictions.

The simple method used in this study has a number of limitations, which suggests that the approach can be refined considerably. First, we partition by MJO and ENSO episodes without consideration of the impact of MJO or ENSO amplitude on the response during those episodes. We expect that the temperature response would increase with MJO and ENSO amplitude, but because the forecasts already exhibit a tendency for overconfidence (Figs. 8a,b), and because a visual examination of lagged temperature composites did not reveal a clear linear relationship with MJO amplitude, we chose not to incorporate additional parameters relating MJO or ENSO amplitude to temperature response. Rodney et al. (2013) provide some evidence that the North American temperature response is, in fact, stronger during strong (RMM amplitude > 2.0) MJO episodes, at least out to lead times of 15 days, which supports the possible usefulness of incorporating amplitude information. Second, we assume that the linear trend is independent of ENSO and the MJO, but changes in frequency of ENSO and even the MJO (Yoo et al. 2011) phases clearly have a substantial influence on the 31-yr linear temperature trend, which we do not consider here. Third, we base the forecasts on the initial state of the MJO, but the MJO itself is predictable out to at least 20 days in state-of-the-art dynamical forecast models (e.g., Vitart and Molteni 2010). Consideration of the predicted state of the MJO may offer another opportunity of refinement.

Perhaps even more fundamental than the limitations mentioned above is that the canonical ENSO and MJO categories used in this and many other studies do not necessarily represent the optimal indices for predicting North American impacts. For example, some MJO states like phases 5 and 6 have a weak relationship with North American temperature (Fig. 5). Schreck et al. (2013) similarly show a weak relationship between North American temperature 6–10 days after the WH04 MJO phase 5, but then show that the phase 5 temperature response is much stronger when further conditioned on a multivariate PNA index that incorporates information on both tropical convection and the extratropical circulation. This example suggests the potential to generate refined forecasts founded on indices that incorporate more background circulation information and that target North American impacts more strongly.

Despite the room for refinement, the evidence of considerable skill in the 2–4-week lead time is encouraging and indicates the opportunity to extend the NOAA/CPC outlooks beyond the 8–14-day period, at least on some occasions. We focus on wintertime, North American temperature in this study because we expect the signal to be strongest in winter owing to the strong Rossby wave source in association with the tight climatological absolute vorticity gradients, the vigorous midlatitude westerlies that promote Rossby wave propagation and synoptic eddy driving, and the seasonal phase locking of ENSO that generally signifies the strongest occurrence of ENSO-related sea surface temperature and tropical convection anomalies in winter. However, the approach adopted here may be attempted for other seasons, other regions, and for other variables such as precipitation. Although the strength of the MJO and ENSO impacts may be reduced in other seasons, the internal atmospheric variability associated with baroclinic eddies also should be reduced, which may allow a comparable signal-to-noise ratio in the extratropics (Trenberth et al. 1998).

Finally, we note that up to this point we have ignored the usefulness of dynamical forecast models in this week 2–4 forecast period, but we expect that many dynamical models should capture the basic MJO- and ENSO-related tropical–extratropical interaction. Riddle et al. (2013) demonstrate that the CFSv2 performs relatively well in capturing the relationship between the MJO and the extratropical circulation in the Pacific–North American region, and Vitart and Molteni (2010) show that the presence of an active MJO improves the days 19–25 forecast performance over the northern extratropics in the ECMWF forecast system. However, these NWP models also may have difficulty simulating some of the observed relationships with the MJO, such as the associated changes in atmospheric blocking frequency (Hamill and Kiladis 2014). Therefore, the forecasts generated through statistical relationships in this study may serve as guidance that complements the information provided by NWP models. The combination of the probabilistic forecasts and the associated skill scores (e.g., Figs. 6 and 7) may inform the forecaster of both the MJO- and ENSO-related enhanced probabilities, as well as the confidence in the forecast. Future work shall focus on means by which statistical forecast guidance, like that of the present study, may be combined with dynamical forecast model output to generate a unified forecast product.

Acknowledgments. We are grateful for support through a grant from the NOAA Climate Test Bed program (Award NA10OAR4310250). We also thank three anonymous reviewers whose comments and suggestions substantially improved this paper.

REFERENCES

Benedict, J. J., S. Lee, and S. B. Feldstein, 2004: Synoptic view of the North Atlantic Oscillation. *J. Atmos. Sci.,* **61,** 121–144.

Branstator, G., 1985: Analysis of general circulation model sea-surface temperature anomaly simulations using a linear model. Part I: Forced solutions. *J. Atmos. Sci.,* **42,** 2225–2241.

Brunet, G., and Coauthors, 2010: Collaboration of the weather and climate communities to advance subseasonal-to-seasonal prediction. *Bull. Amer. Meteor. Soc.,* **91,** 1397–1406.

Bukovsky, M. S., 2012: Temperature trends in the NARCCAP regional climate models. *J. Climate,* **25,** 3985–3991.

Cassou, C., 2008: Intraseasonal interaction between the Madden–Julian oscillation and North Atlantic Oscillation. *Nature,* **455,** 523–527, doi:10.1038/nature07286.

Dee, D. P., and Coauthors, 2011: The ERA-Interim reanalysis: Configuration and performance of the data assimilation system. *Quart. J. Roy. Meteor. Soc.,* **137,** 553–597.

Feldstein, S. B., 2002: Fundamental mechanisms of the growth and decay of the PNA teleconnection pattern. *Quart. J. Roy. Meteor. Soc.,* **128,** 775–796.

Ferranti, L., T. N. Palmer, F. Molteni, and E. Klinker, 1990: Tropical–extratropical interaction associated with the 30–60 day oscillation and its impact on medium and extended range prediction. *J. Atmos. Sci.,* **47,** 2177–2199.

Franzke, C., S. B. Feldstein, and S. Lee, 2011: Synoptic analysis of the Pacific–North American teleconnection pattern. *Quart. J. Roy. Meteor. Soc.,* **137,** 329–346.

Garfinkel, C. I., S. B. Feldstein, D. W. Waugh, C. Yoo, and S. Lee, 2012: Observed connection between stratospheric sudden warmings and the Madden–Julian oscillation. *Geophys. Res. Lett.,* **39,** L18807, doi:10.1029/2012GL053144.

Gottschalck, J., and Coauthors, 2010: A framework for assessing operational Madden–Julian oscillation forecasts: A CLIVAR MJO Working Group project. *Bull. Amer. Meteor. Soc.,* **91,** 1247–1258.

Halpert, M. S., and C. F. Ropelewski, 1992: Surface temperature patterns associated with the Southern Oscillation. *J. Climate,* **5,** 577–593.

Hamill, T. M., and G. N. Kiladis, 2014: Skill of the MJO and Northern Hemisphere blocking in GEFS medium-range reforecasts. *Mon. Wea. Rev.,* in press.

Higgins, R. W., and K. C. Mo, 1997: Persistent North Pacific circulation anomalies and the tropical intraseasonal oscillation. *J. Climate,* **10,** 223–244.

Hoskins, B. J., 2013: The potential for skill across the range of the seamless weather–climate problem: A stimulus for our science. *Quart. J. Roy. Meteor. Soc.,* **139,** 573–584.

——, and D. J. Karoly, 1981: The steady linear response of a spherical atmosphere to thermal and orographic forcing. *J. Atmos. Sci.,* **38,** 1179–1196.

Hsu, H.-H., 1996: Global view of the intraseasonal oscillation during northern winter. *J. Climate,* **9,** 2386–2406.

Hurrell, J. W., Y. Kushnir, M. Visbeck, and G. Ottersen, 2003: An overview of the North Atlantic Oscillation. *The North Atlantic Oscillation: Climate Significance and Environmental Impact, Geophys. Monogr.,* Vol. 134, Amer. Geophys. Union, 1–35.

Jin, F., and B. J. Hoskins, 1995: The direct response to tropical heating in a baroclinic atmosphere. *J. Atmos. Sci.,* **52,** 307–319.

Johnson, N. C., and S. B. Feldstein, 2010: The continuum of North Pacific sea level pressure patterns: Intraseasonal, interannual, and interdecadal variability. *J. Climate,* **23,** 851–867.

Jones, C., L. M. V. Carvalho, J. Gottschalck, and W. Higgins, 2011: The Madden–Julian oscillation and the relative value of deterministic forecasts of extreme precipitation in the contiguous United States. *J. Climate,* **24,** 2421–2428.

Knutson, T. R., and K. M. Weickmann, 1987: 30–60 day atmospheric oscillations: Composite life cycles of convection and circulation anomalies. *Mon. Wea. Rev.,* **115,** 1407–1436.

Kumar, A., 2009: Finite samples and uncertainty estimates for skill measures for seasonal prediction. *Mon. Wea. Rev.,* **137,** 2622–2631.

Lee, S., T. Gong, N. Johnson, S. B. Feldstein, and D. Pollard, 2011: On the possible link between tropical convection and the Northern Hemisphere Arctic surface air temperature change between 1958 and 2001. *J. Climate,* **24,** 4350–4367.

L'Heureux, M. L., and D. W. J. Thompson, 2006: Observed relationships between the El Niño–Southern Oscillation and the extratropical zonal-mean circulation. *J. Climate,* **19,** 276–287.

——, and R. W. Higgins, 2008: Boreal winter links between the Madden–Julian oscillation and the Arctic Oscillation. *J. Climate,* **21,** 3040–3050.

Lin, H., and G. Brunet, 2009: The influence of the Madden–Julian oscillation on Canadian wintertime surface air temperature. *Mon. Wea. Rev.,* **137,** 2250–2262.

——, ——, and J. Derome, 2009: An observed connection between the North Atlantic Oscillation and the Madden–Julian oscillation. *J. Climate,* **22,** 364–380.

——, ——, and R. Mo, 2010: Impact of the Madden–Julian oscillation on wintertime precipitation in Canada. *Mon. Wea. Rev.,* **138,** 3822–3839.

Madden, R. A., and P. R. Julian, 1971: Detection of a 40–50 day oscillation in the zonal wind in the tropical Pacific. *J. Atmos. Sci.,* **28,** 702–708.

——, and ——, 1972: Description of global-scale circulation cells in the tropics with a 40–50 day period. *J. Atmos. Sci.,* **29,** 1109–1123.

Matthews, A. J., B. J. Hoskins, and M. Masutani, 2004: The global response to tropical heating in the Madden–Julian oscillation during the northern winter. *Quart. J. Roy. Meteor. Soc.,* **130,** 1991–2011.

Moon, J.-Y., B. Wang, and K.-J. Ha, 2011: ENSO regulation of MJO teleconnection. *Climate Dyn.,* **37,** 1133–1149.

Moore, R. W., O. Martius, and T. Spengler, 2010: The modulation of the subtropical and extratropical atmosphere in the Pacific basin in response to the Madden–Julian oscillation. *Mon. Wea. Rev.,* **138,** 2761–2778.

Mori, M., and M. Watanabe, 2008: The growth and triggering mechanisms of the PNA: A MJO–PNA coherence. *J. Meteor. Soc. Japan,* **86,** 213–236.

Newman, M., and P. D. Sardeshmukh, 2008: Tropical and stratospheric influences on extratropical short-term climate variability. *J. Climate,* **21,** 4326–4347.

Riddle, E. E., M. B. Stoner, N. C. Johnson, M. L. L'Heureux, D. C. Collins, and S. B. Feldstein, 2013: The impact of the MJO on clusters of wintertime circulation anomalies over the North American region. *Climate Dyn.,* **40,** 1749–1766.

Rodney, M., H. Lin, and J. Derome, 2013: Subseasonal prediction of wintertime North American surface air temperature during strong MJO events. *Mon. Wea. Rev.,* **141,** 2897–2909.

Ropelewski, C. F., and M. S. Halpert, 1987: Global and regional scale precipitation patterns associated with the El Niño/Southern Oscillation. *Mon. Wea. Rev.,* **115,** 1606–1626.

Roundy, P. E., and L. M. Gribble-Verhagen, 2010: Variations in the flow of the global atmosphere associated with a composite convectively coupled oceanic Kelvin wave. *J. Climate,* **23,** 4192–4201.

——, K. MacRitchie, J. Asuma, and T. Melino, 2010: Modulation of the global atmospheric circulation by combined activity in the Madden–Julian oscillation and the El Niño–Southern Oscillation during boreal winter. *J. Climate,* **23,** 4045–4059.

Saha, S., and Coauthors, 2014: The NCEP Climate Forecast System version 2. *J. Climate,* in press.

Sardeshmukh, P. D., and B. J. Hoskins, 1988: The generation of global rotational flow by steady idealized tropical divergence. *J. Atmos. Sci.,* **45,** 1228–1251.

Schrage, J. M., D. G. Vincent, and A. H. Fink, 1999: Modulation of intraseasonal (25–70 day) processes by the superimposed ENSO cycle across the Pacific basin. *Meteor. Atmos. Phys.,* **70,** 15–27.

Schreck, C. J., J. M. Cordeira, and D. Margolin, 2013: Which MJO events affect North American temperatures? *Mon. Wea. Rev.,* **141,** 3840–3850.

Simmons, A. J., J. M. Wallace, and G. W. Branstator, 1983: Barotropic wave propagation and instability, and atmospheric teleconnection patterns. *J. Atmos. Sci.,* **40,** 1363–1392.

Tam, C.-Y., and N.-C. Lau, 2005: The impact of ENSO on atmospheric intraseasonal variability as inferred from observations and GCM simulations. *J. Climate,* **18,** 1902–1924.

Ting, M., and P. D. Sardeshmukh, 1993: Factors determining the extratropical response to equatorial diabatic heating anomalies. *J. Atmos. Sci.,* **50,** 907–918.

Trenberth, K. E., and J. M. Caron, 2000: The Southern Oscillation revisited: Sea level pressures, surface temperatures, and precipitation. *J. Climate,* **13,** 4358–4365.

——, G. W. Branstator, D. Karoly, A. Kumar, N.-G. Lau, and C. Ropelewski, 1998: Progress during TOGA in understanding and modeling global teleconnections associated with tropical sea surface temperatures. *J. Geophys. Res.,* **103** (C7), 14 291–14 324.

Vecchi, G. A., and N. A. Bond, 2004: The Madden–Julian oscillation (MJO) and northern high latitude wintertime surface air temperatures. *Geophys. Res. Lett.,* **31,** L04104, doi:10.1029/2003GL018645.

Vitart, F., and F. Molteni, 2010: Simulation of the Madden–Julian oscillation and its teleconnections in the ECMWF forecast system. *Quart. J. Roy. Meteor. Soc.,* **136,** 842–855.

Wheeler, M. C., and H. H. Hendon, 2004: An all-season real-time multivariate MJO index: Development of an index for monitoring and prediction. *Mon. Wea. Rev.,* **132,** 1917–1932.

Wilks, D. S., 2011: *Statistical Methods in the Atmospheric Sciences.* Elsevier, 676 pp.

Yao, W., H. Lin, and J. Derome, 2011: Submonthly forecasting of winter surface air temperature in North America based on organized tropical convection. *Atmos.–Ocean,* **49,** 51–60.

Yoo, C., S. Feldstein, and S. Lee, 2011: The impacts of the Madden–Julian oscillation trend on the Arctic amplification of surface air temperature during the 1979–2008 boreal winter. *Geophys. Res. Lett.,* **38,** L24804, doi:10.1029/2011GL049881.

——, S. Lee, and S. B. Feldstein, 2012: Mechanisms of Arctic surface air temperature change in response to the Madden–Julian oscillation. *J. Climate,* **25,** 5777–5790.

Zhang, C., 2005: Madden–Julian oscillation. *Rev. Geophys.,* **43,** RG2003, doi:10.1029/2004RG000158.

——, 2013: Madden–Julian oscillation: Bridging weather and climate. *Bull. Amer. Meteor. Soc.,* **94,** 1849–1870.

Zhou, S., M. L. L'Heureux, S. Weaver, and A. Kumar, 2012: A composite study of the MJO influence on the surface air temperature and precipitation over the continental United States. *Climate Dyn.,* **38,** 1459–1471.